Analyst

Accepted Manuscript

ROYAL SOCIETY OF CHEMISTRY

www.rsc.org/analyst

Facile synthesis of porous bimetallic alloyed PdAg nanoflowers supported on reduced graphene oxide for simultaneous detection of ascorbic acid, dopamine, and uric acid

Li-Xian Chen, Jie-Ning Zheng, Ai-Jun Wang,* Lan-Ju Wu, Jian-Rong Chen, Jiu-Ju Feng*

College of Geography and Environmental Science, College of Chemistry and Life Science, Zhejiang Normal University, Jinhua, 321000, China

**Corresponding author: ajwang@znju.cn(AJW); jjfeng@zjnu.cn(JJF); Tel./Fax: +86 579 82282269.*

Abstract

Porous bimetallic alloyed PdAg nanoflowers supported on reduced graphene oxide (PdAg NFs/rGO) were prepared via a facile and simple in-situ reduction process, with the assistance of cetyltrimethylammonium bromide (CTAB) as a structure-directing agent. The as-prepared nanocomposites modified glassy carbon electrode (denoted as PdAg NFs/rGO/GCE) showed enhanced catalytic currents and enlarged peak potential separations for the oxidation of ascorbic acid (AA), dopamine (DA), and uric acid (UA) as compared to PdAg/GCE, rGO/GCE, commercial Pd/C/GCE, and bare GCE. The as-developed sensor was explored for selective detection of AA, DA, and UA with good anti-interference ability, wide linear ranges of 1.0 μM~2.1 mM, 0.4~96.0 μM, and 1.0~150.0 μM, along with low detection limits of 0.057, 0.048, and 0.081 μM (*S*/*N* = 3), respectively. For simultaneous detection of AA, DA, and UA, the corresponding linear ranges were 1.0 μM~4.1 mM, 0.05~112.0 μM, and 3.0~186.0 μM, with the detection limits of 0.185, 0.017, and 0.654 μM (S/N = 3), respectively.

Keywords: Reduced graphene oxide; Bimetallic alloy; Simultaneous detection; Ascorbic acid; Dopamine; Uric acid

Introduction

Ascorbic acid (AA) is familiar with its antioxidant feature, which plays a critical role in several physiological processes such as gene expression and cell division.[1] Dopamine (DA) is an important neurotransmitter existed in mammalian central nervous system, whose abnormal levels would cause neurological disorder such as schizophrenia and Parkinson's disease.[2] Uric acid (UA) is the primary end product of purine metabolism. Its abnormal concentration levels will induce several diseases, including pneumonia, gout, and hyper-uricemia.[3] As well known, AA, DA, and UA are usually coexisted in real biological samples and thereby it is highly necessary to develop a novel method for their selective and/or simultaneous determination.

Electrochemical methods have the advantages of low cost, rapidity, convenience, high sensitivity, and selectivity, and thus attract increasing attention for simultaneous determination of electroactive small molecules.[4-6] However, it is very difficult for accurate detection of AA, DA, and UA, owing to their overlapped oxidation peaks on bare electrodes and severe electrode fouling effects.[7] To overcome these disadvantages, a variety of advanced materials have been employed to modify the electrode surfaces such as organic redox mediators,[8, 9] polymers,[10, 11] metal complexes or nanoparticles,[12-15] and carbon-based materials.[16-18] Among them, carbon materials such as graphene and carbon nanotubes (CNTs) are most widely used for

simultaneous determination of AA, DA, and UA.[19]

Recently, graphene has attracted tremendous interest because of its good electrical conductivity, large specific surface area, strong mechanical strength, and superior chemical activity.[20-23] Studies demonstrate that graphene-based modified electrodes have higher catalytic activity [24, 25] and electrical conductivity,[25] as well as wide applications for simultaneous detection of AA, DA, and UA. For example, Xia and co-workers prepared nitrogen doped graphene with enhanced catalytic activity for AA, DA, and UA oxidation.[18] Qu et al. fabricated porphyrin-functionalized graphene for DA detection with high selectivity and sensitivity.[26] Niu's group synthesized chitosan functionalized graphene and used for selective detection of AA, DA, and UA.[27]

Meanwhile, noble metal nanomaterials have broad applications in catalysis and electrochemical sensors, owing to their unique physical and chemical properties.[6, 28, 29] More importantly, bimetallic nanostructures display improved catalytic performances for their synergistic effects and controllable compositions as contrast to monometallic counterparts.[30] For instance, PdCr alloyed nanoparticles exhibited enhanced catalytic activity toward H_2O_2 and glucose oxidation, compared with Pd nanoparticles and Pt/C.[31] In another example, alloyed Pt_3Co nanoflowers showed improved catalytic activity for methanol oxidation and oxygen reduction, using commercial Pt black as a reference.[32]

For simultaneous determination of AA, DA, and UA with high sensitivity and good selectivity, it is effective to use graphene as a support to immobilize bimetallic

nanoparticles on the electrode surface. Jiang et al. synthesized poly(diallyldimethylammonium chloride) (PDDA) functionalized reduced graphene oxide (rGO) supported PdPt nanoparticles for simultaneous determination of DA, UA, and AA.[33] And PdPt/PDDA-rGO modified electrode showed well-separated oxidation peaks and much enlarged oxidation currents, compared to that of PDDA-rGO. Du and coworkers fabricated rGO-supported Au@Pd nanostructures for simultaneous detection of AA, DA, and UA with low detection limits and wide concentration ranges.[34]

In this work, a simple in-situ reduction method was developed for synthesis of rGO supported porous alloyed PdAg nanocomposites (PdAg NFs/rGO), with the assistance of cetyltrimethylammonium bromide (CTAB) as a structure-directing agent. The electrocatalytic performances of PdAg NFs/rGO modified electrodes were investigated in some detail, using the detection of AA, DA, and UA as model systems.

2. Experimental section

2.1 Chemicals

Graphite powder (8000 meshes), palladium chloride ($PdCl_2$), silver nitrate ($AgNO_3$), cetyltrimethylammonium bromide (CTAB), and ascorbic acid (AA) were purchased from Aladdin Company (Shanghai, China). All the other chemicals were of analytical grade and used without further purification. All the aqueous solutions were prepared with twice-distilled water in the whole experiments.

2.2 Preparation of rGO

Graphene oxide (GO) was synthesized from graphite powder based on a modified Hummers' method.[35] To obtain exfoliated GO, the as-prepared GO dispersion was sonicated for 0.5 h.

For typical preparation of rGO, 2 mg of the as-synthesized GO was dispersed in 2 mL of water by ultrasonication, followed by the addition of 3 mL of 0.1 M AA. Then, the mixture was treated in water bath at 60 °C for 100 min under stirring. The mixture gradually turned black, resulting in the formation of rGO. The residual AA was removed by centrifugation and thoroughly washed with water. The as-obtained precipitates were re-dispersed in water for further characterization.

2.3 Synthesis of PdAg NFs/rGO

Typically, 50 μL of rGO (1 mg mL^{-1}) was mixed with 2 mL of CTAB (0.25 mM) under stirring. Then, 40 uL of $AgNO_3$ (10 mM) and 4 uL of H_2PdCl_4 (100 mM) were simultaneously dispersed into the mixture via stirring, followed by the addition of 16 uL of 0.1 M AA. The mixture became dark brown within several minutes and then put into a water bath (30 °C) for further reaction of 2 h.

For comparison, other PdAg samples were prepared in the absence of rGO (denoted as PdAg) or changing CTAB concentrations, while other experimental conditions were kept constant.

2.4 Characterization

Transmission electron microscopy (TEM), high-resolution TEM (HRTEM), high-angle annular dark-field scanning transmission electron microscopy (HAADF-STEM), elemental mapping, selected area electron diffraction (SAED) analysis, and energy-dispersive X-ray spectroscopy (EDS) were performed on a JEM-2100F microscope operated at 200 kV. X-ray diffraction (XRD) spectra were recorded on a Rigaku Dmax-2000 diffractometer using Cu Kα radiation source (λ = 0.15418 nm). X-ray photoelectron spectroscopy (XPS) measurements were conducted on a K-Alpha XPS (ThermoFisher, E. Grinstead, UK) with an Al Kα X-ray radiation (1486.6 eV photons) for excitation operated at 120 W. Specific surface area was estimated by Brunauer-Emmett-Teller (BET) nitrogen adsorption-desorption on a Surface Area Analyzer (NOVA2000-09, USA) at 77.3 K. The sample was dried at 90 °C for 4 h and then degassed at 300 °C for 1 h before determination. Raman spectra were acquired on a Renishaw Raman system model 1000 spectrometer equipped with a CCD detector, carried with a He/Ne laser at a wavelength of 633 nm. Thermogravimetric analysis (TGA) was performed in air on a NETZSCH STA 449C thermogravimetric analyzer. The samples were heated from 25 to 900 °C with the heat rate of 10 °C min^{-1}.

2.5 Electrochemical measurements

All the electrochemical measurements were performed in a traditional three-electrode cell using a CHI660D electrochemical workstation (CH Instruments, Chenhua Co., Shanghai, China) with a bare or modified glassy carbon electrode (GCE,

3 mm in diameter) as the working electrode, an Ag/AgCl electrode as the reference electrode, and a platinum wire as the counter electrode. All the potentials were expressed with respect to the Ag/AgCl electrode.

For typical fabrication of PdAg NFs/rGO modified GCE (denoted as PdAg NFs/rGO/GCE), 5.0 mg of the sample was dispersed in 5.0 mL of water under ultrasonication for 30 min. Then, 6 μL of the suspension was uniformly dropped onto the electrode surface, and dried naturally, followed by casting 4 μL of Nafion ionomers (0.05 wt%). For comparison, rGO, PdAg, and commercial Pd/C modified electrodes were prepared in a similar way.

3. Results and discussion

3.1. Characterization of PdAg NFs/rGO

Low-resolution TEM image (Fig. 1A) shows that the typical product is composed of many well-defined nanoflowers uniformly dispersed on rGO surface, with an average size of 38.92 nm (inset in Fig. 1A). The middle-resolution TEM image verifies the porous structures of the product (Fig. 1B), and their polycrystalline nature is demonstrated by the corresponding SAED pattern (inset in Fig. 1B). HRTEM image reveals well-defined lattice fringes throughout an individual nanoflower (Fig. 1C), suggesting good crystallinity of porous PdAg NFs. The interplanar spacing is estimated to be 0.230 nm (Fig. 1D, E), as determined from the marked regions (Fig. 1C), which is smaller than that of the (111) lattice spacing of the face-centered cubic (fcc) Ag (0.236 nm, JCPDS-04-0783), but larger than that of the

fcc Pd (0.225 nm, JCPDS-46-1043), indicating the formation of the fcc PdAg alloy. Additionally, Fig. 1A clearly shows the wrinkles of rGO nanosheets (denoted by the arrows), confirming the existence of rGO.

HAADF-STEM elemental mapping images (Fig. 2A) and the corresponding elemental line scanning profiles (Fig. 2B) show a homogeneous distribution of Pd and Ag in a single porous PdAg nanoflower, which further manifests the alloyed feature of PdAg NFs. Furthermore, EDS analysis confirms the coexistence of Pd and Ag. And the atomic ratio of Pd to Ag is around 56.09:43.91, which is close to the stoichiometric ratio (1:1) of H_2PdCl_4 and $AgNO_3$ (Fig. S1, Electronic Supplementary Information, ESI).

Fig. 3 shows the XRD patterns of PdAg NFs/rGO (curve a), GO (curve b), bulk Pd (JCPDS-46-1043), and Ag (JCPDS-04-0783). There are five representative diffraction peaks at 39.80°, 46.34°, 67.88°, 81.57°, and 85.95° for PdAg NFs/rGO, which are indexed to the (111), (200), (220), (311), and (222) planes of fcc PdAg alloy.[36] Furthermore, these peaks coincidentally locate between the positions of bulk Pd and Ag, further verifying the formation of PdAg alloys. In addition, the sharp peak of GO at 11.0° is corresponding to the (002) planes with the interplanar spacing of 0.85 nm. This value is larger than that of pristine graphite (0.34 nm), owing to the insertion of oxygenated functional groups between layers.[37] After reduction by AA, the diffraction peak of the (002) planes becomes broader and red shifts to 22.5° for PdAg NFs/rGO, suggesting the effective reduction of GO to rGO.[38]

The oxidation states and compositions of PdAg NFs/rGO were determined by

XPS measurements (Fig. 4). Survey XPS spectrum confirms the coexistence of Pd, Ag, C and O elements in PdAg NFs/rGO (Fig. 4A). The oxidation states of Pd and Ag can be obtained by fitting the peaks in high-resolution Pd 3d and Ag 3d XPS spectra (Fig. 4B and C). Obviously, there are only Pd^0 and Ag^0 detected, indicating the efficient reduction of $PdCl_4^{2-}$ and Ag^+ to metallic Pd and Ag, respectively. Besides, the peak at around 285.1 eV is corresponding to C 1s (Figure 4D), which is divided into four peaks at 284.38, 284.91, 286.42, and 288.56 eV, corresponding to C–C (sp^2), C–O, C=O, and O–C=O groups, respectively.[39] Impressively, the oxygenated functional groups significantly decrease for PdAg NFs/rGO, compared with those of GO (Fig. S2, ESI), revealing the efficient reduction of GO to rGO.[40]

Nitrogen adsorption measurements were conducted to provide the information on the surface area and porosity properties of PdAg NFs/rGO (Fig. 5). The nitrogen adsorption-desorption isotherm curves measured at 77.35K exhibits a distinct hysteresis loop at a relative pressure P/P_0 ranging from 0.14 to 0.45. Besides, the N_2 physisorption isotherm is essentially a type IV curve, which indicates the typical porous characteristic of PdAg NFs/rGO. The BET surface area of porous PdAg NFs/rGO is 15.91 $m^2\ g^{-1}$.

Raman analysis was performed to examine the structural changes during the reduction process from GO to rGO. Fig. S3A (ESI) provides Raman spectra of PdAg NFs/rGO (curve a) and GO (curve b). The two distinguished peaks at around 1335 and 1590 cm^{-1} correspond to the *D* band associated with the order/disorder of graphite structure and *G* band related with the graphitic stacking structure.[41] The *D*/*G*

intensity ratio is an indicator of the average size of the in-plane sp^2 domains and degree of disorder.[42] The *D*/*G* intensity ratio is 1.12 for PdAg NFs/rGO, which is larger than that of GO (0.82), demonstrating the formation of smaller in-plane sp^2 domains and partially ordered crystal structures during the reduction of GO and further verifying the formation of graphene.[39]

The metal loading of PdAg NFs/rGO was obtained based on TGA analysis (Fig. S3B, curve a, ESI). The weight loss below 100 °C is attributed to the removal of water molecules adsorbed between rGO nanosheets.[43, 44] The steady weight loss in the temperature range of 200~500 °C is assigned to pyrolysis of oxygenated functional groups,[43, 44] which is much lower than that of GO (curve b). It reveals the decrease of the oxygenated functional groups in rGO. And a sharp mass drop is emerged at around 600 °C, which is caused by the combustion of carbon skeleton of rGO.[43, 44] Additionally, the metal mass loading is 60.1 %, which is evaluated from the remained mass loading of PdAg NFs/rGO.

Controlled experiments demonstrate that both rGO and the amount of CTAB play essential roles in the formation of well-dispersed porous PdAg NFs. The absence of rGO yields heavily aggregated PdAg NFs (Fig. S4, ESI), even the other conditions were kept constant. It means the critical role of rGO for well-dispersed porous PdAg NFs.

Besides, the concentrations of CTAB are important for synthesis of porous PdAg NFs (Fig. S5, ESI). The absence of CTAB yields irregular solid nanoparticles (Fig. S5A), which is different from those of the best PdAg NFs prepared with 0.25 mM

CTAB (Fig. 1A). The porous structures are still remained by using 0.80 mM CTAB, while their quality slightly drops down (Fig. S5B). Increasing the concentration up to 10 mM induces the formation of solid PdAg nanoparticles(Fig. S5C). Therefore, CTAB is important in morphology-controlled synthesis, which greatly influences the reaction rate. For example, the reaction is completed within 2 h in the presence of 0.25 mM CTAB, while it takes more than 24 h with 10 mM CTAB. According to the previous work,[45] anisotropic nanostructures can be formed at weak driving force by layer-by-layer growth. Alternatively, porous structures would emerge at stronger driving forces controlled by continuous growth.

3.2. Electrooxidation behaviors of AA, DA, and UA

Prior to electrochemical measurements, we investigated the pH effects on the electrochemical responses of PdAg NFs/rGO/GCE for determination of AA, DA, and UA (Fig. S6). Considering the peak currents and the anodic peak potential separations (ΔE_p) for the oxidation of AA, DA, and UA, pH 6.0 was chosen as the optimal pH value for subsequent tests.

Fig. 6A-C show the CV curves recorded on PdAg NFs/rGO/GCE (curve a), PdAg/GCE (curve b), rGO/GCE (curve c), Pd/C/GCE (curve d), and bare GCE (inset) in 0.1 M phosphate solutions (pH 6.0) containing 4 mM AA, 0.2 mM DA, and 1 mM UA. For AA oxidation (Fig. 6A), an enlarged peak is found at 0.048 V on PdAg NFs/rGO/GCE, which is distinctively different from that on bare GCE with a small and sluggish peak detected at 0.987 V. For DA oxidation (Fig. 6B), the oxidation and

reduction peak potentials are located at 235 and 187 mV on PdAg NFs/rGO/GCE, while they are observed at 511 and 4 mV on bare GCE. The ΔE_P are 48 and 507 mV for PdAg NFs/rGO/GCE and bare GCE, respectively, revealing that the reversibility of the redox of DA is obviously improved on PdAg NFs/rGO/GCE. In the case of UA (Fig. 6C), a strong oxidation peak appears at 0.369 V on PdAg NFs/rGO/GCE, and it shifts to 0.962 V with a steeply decreased peak current on bare GCE. In addition, the oxidation peak currents of AA, DA, and UA significantly increase on PdAg NFs/rGO/GCE, compared to those on PdAg/GCE, rGO/GCE, Pd/C/GCE, and bare GCE.

Differential pulse voltammetry (DPV) was employed for simultaneous determination of AA, DA, and UA for its higher sensitivity and lower detection limit.[4] Fig. 6D shows the DPV curves of PdAg NFs/rGO/GCE (curve a), PdAg/GCE (curve b), rGO/GCE (curve c), Pd/C/GCE (curve d), and bare GCE (curve e) in 0.1 M phosphate solutions (pH 6.0) containing 1.1 mM AA, 22.0 μM DA, and 185.0 μM UA. Notably, three well-defined peaks are found at -0.040, 0.164, and 0.292 V on PdAg NFs/rGO/GCE. And the ΔE_P values of AA–DA, DA–UA, and AA–UA are 0.204, 0.128, and 0.332 V, respectively, which are big enough to determine AA, DA, and UA simultaneously in the present case. However, bare GCE and PdAg/GCE display two weak and broad oxidation peaks with partially overlapping for AA, DA, and UA oxidation.

Although the DPV behaviors of AA, DA, and UA on rGO/GCE and Pd/C/GCE are similar to those on PdAg NFs/rGO/GCE, while their oxidation peak currents are

smaller. Taken the large peak separations and the enhanced currents together, PdAg NFs/rGO/GCE is the best for the simultaneous detection of AA, DA, and UA.

3.3 Selective and simultaneous detection of AA, DA, and UA

Fig. 7A depicts the DPV curves obtained on PdAg NFs/rGO/GCE in 0.1 M phosphate solutions in the presence of 4.0 μM DA and 40.0 μM UA by varying AA concentration from 1.0 μM to 2.1 mM. The oxidation peak currents increase linearly with AA concentrations, while those of DA and UA keep almost unchanged. Similar trends are observed for the detection of DA (Fig. 7B) and UA (Fig. 7C) with the linear concentration ranges of 0.4~96.0 μM and 1.0~150.0 μM, respectively.

The detection limits of AA, DA, and UA are 0.057, 0.048, and 0.081 μM (S/N = 3), respectively. The DPV behaviors of PdAg NFs/rGO/GCE were also investigated for simultaneous detection of AA, DA, and UA with different concentrations. The oxidation peak currents increase linearly with the concentrations of AA, DA, and UA (Fig. 8). The linear concentration ranges are 1.0 μM to 4.1 mM, 0.05 to 112.0 μM, and 3.0 to 186.0 μM for AA, DA, and UA, with the detection limits of 0.185, 0.017, and 0.654 μM (S/N = 3), respectively. As displayed in Table S1 and S2 (ESI), by comparing the analytical parameters such as detection limit and linear range, and ΔE_P, PdAg NFs/rGO/GCE shows better or comparable properties to the nanomaterials used for the determination of AA, DA, and UA in the literature. Evidently, PdAg NFs/rGO/GCE exhibits better or comparable features for AA, DA, and UA oxidation. This is ascribed to the following reasons: (1) porous structures of PdAg NFs that

contributes larger surface area; (2) high content and better dispersion of PdAg NFs on rGO nanosheets that enlarges surface area and facilitates electron transfer; (3) excellent electrocatalytic activity of rGO and PdAg NFs toward AA, DA, and UA oxidation.[18] As a result, PdAg NFs/rGO/GCE is a potential candidate for AA, DA, and UA biosensor. Moreover, it is worth mentioning that the electrochemical behavior of PdAg NFs/rGO/GCE is superior compared with similarly designed biosensors in literature comprised of utilize bimetallic nanoparticles,[46-48] nanoparticles on graphene/graphene oxide,[33, 34, 49] and flower-like catalysts immobilized on oxides/insulators.[50]

3.4 Reproducibility and stability of PdAg NFs/rGO/GCE

The reproducibility of PdAg NFs/rGO/GCE was tested by DPV measurements in 0.1 M phosphate solutions (pH 6.0) containing 1.1 mM AA, 22.0 μM DA, and 185.0 μM UA. The relative standard deviations (RSDs) are around 1.99%, 1.02%, and 2.52% for AA, DA, and UA, respectively, after 20 successive DPV runs. The stability of PdAg NFs/rGO/GCE was studied by keeping it in phosphate solutions (pH 6.0) for one month in refrigerator. The oxidation peak currents of AA, DA, and UA only decreased 8.24% for AA, 6.35% for DA, and 9.16% for UA. These results demonstrate acceptable reproducibility and good stability of PdAg NFs/rGO/GCE for AA, DA, and UA detection.

3.5 Interference test

We investigated the possible interferences of some inorganic ions and several small molecules with the concentration of 1 mM in 0.1 M phosphate solutions (pH 6.0) containing 50.0 μM AA, 10.0 μM DA, and 20.0 μM UA (Fig. 9). No interference was found in the presence of citric acid, glycine, CO_3^{2-}, NO_3^-, glucose, and lysine. The oxidation potential of acetaminophen is 0.51 V at PdAg NFs/rGO/GCE. 250 folds of acetaminophen have no interference with the determination of DA and AA because of their different oxidation potentials. However, acetaminophen might cause a little interference on the detection of UA under the same conditions. It was found that RSDs of the determination of UA is 3.75% (n = 3) in the presence of 50 folds of acetaminophen. These results strongly demonstrate that the as-prepared PdAg NFs/rGO modified electrode have high selectivity and anti-interference.

4. Conclusions

A novel sensor was fabricated based on reduced graphene oxide supported well-dispersed porous bimetallic alloyed PdAg nanoflowers by a simple in-situ reduction. PdAg NFs/rGO/GCE showed the improved catalytic activity toward AA, DA, and UA oxidation, displaying larger peak separations and enhanced peak currents for the oxidation of the three analytes. The as-developed sensor was applied for selective and simultaneous detection of AA, DA, and UA with good selectivity (0.204, 0.128, and 0.332 V for the oxidation peak potentials separations of AA–DA, DA–UA, and AA–UA), high sensitivity, low detection limits (0.185, 0.017, and 0.654 μM for AA, DA, and UA in the simultaneous detection), and wide linear concentration ranges

(1.0 μM to 4.1 mM, 0.05 to 112.0 μM, and 3.0 to 186.0 μM for AA, DA, and UA in the simultaneous detection). The enhanced performance should be ascribed to the unique structure of porous alloyed PdAg NFs and synergistic effects between rGO and PdAg NFs. The fabricated PdAg NFs/rGO/GCE will be a promising electrochemical sensor for a wide scope of electrochemical sensing and biosensing applications for the detection of different biomolecules.

Acknowledgement

This work was financially supported by National Natural Science Foundation of China (Nos. 21475118, 21175118, 21275130 and 21275131), Zhejiang province university young academic leaders of academic climbing project (No. pd2013055) and Zhejiang province environmental protection scientific research plan project (2013A025).

References

1. L. Yang, D. Liu, J. Huang and T. You, *Sens. Actuators, B*, 2014, **193**, 166-172.
2. J. Huang, Y. Liu, H. Hou and T. You, *Biosens. Bioelectron.*, 2008, **24**, 632-637.
3. M. Mallesha, R. Manjunatha, C. Nethravathi, G. S. Suresh, M. Rajamathi, J. S. Melo and T. V. Venkatesha, *Bioelectrochemistry*, 2011, **81**, 104-108.
4. T.-Q. Xu, Q.-L. Zhang, J.-N. Zheng, Z.-Y. Lv, J. Wei, A.-J. Wang and J.-J. Feng, *Electrochim. Acta*, 2014, **115**, 109-115.

5. K.-J. Chen, C.-F. Lee, J. Rick, S.-H. Wang, C.-C. Liu and B.-J. Hwang, *Biosens. Bioelectron.*, 2012, **33**, 75-81.

6. Q. Kang, L. Yang and Q. Cai, *Bioelectrochemistry*, 2008, **74**, 62-65.

7. Z. Gao and H. Huang, *Chem. Commun.*, 1998, 2107-2108.

8. S. Shahrokhian and M. Ghalkhani, *Electrochim. Acta*, 2006, **51**, 2599-2606.

9. H. R. Zare, N. Nasirizadeh and M. Mazloum Ardakani, *J. Electroanal. Chem.*, 2005, **577**, 25-33.

10. J. Chen, J. Zhang, X. Lin, H. Wan and S. Zhang, *Electroanalysis*, 2007, **19**, 612-615.

11. Y. Li and X. Lin, *Sens. Actuators, B*, 2006, **115**, 134-139.

12. P. Shakkthivel and S.-M. Chen, *Biosens. Bioelectron.*, 2007, **22**, 1680-1687.

13. S. Shahrokhian and H. R. Zare-Mehrjardi, *Sens. Actuators, B*, 2007, **121**, 530-537.

14. P. Wang, Y. Li, X. Huang and L. Wang, *Talanta*, 2007, **73**, 431-437.

15. L. Zhang and X. Jiang, *J. Electroanal. Chem.*, 2005, **583**, 292-299.

16. R. Cui, X. Wang, G. Zhang and C. Wang, *Sens. Actuators, B*, 2012, **161**, 1139-1143.

17. Y. Liu, J. Huang, H. Hou and T. You, *Electrochem. Commun.*, 2008, **10**, 1431-1434.

18. Z.-H. Sheng, X.-Q. Zheng, J.-Y. Xu, W.-J. Bao, F.-B. Wang and X.-H. Xia, *Biosens. Bioelectron.*, 2012, **34**, 125-131.

19. Y. Shao, J. Wang, H. Wu, J. Liu, I. A. Aksay and Y. Lin, *Electroanalysis*, 2010, **22**, 1027-1036.

20. J.-N. Zheng, S.-S. Li, F.-Y. Chen, N. Bao, A.-J. Wang, J.-R. Chen and J.-J. Feng, *J. Power Sources*, 2014, **266**, 259-267.

21. X. Huang, X. Qi, F. Boey and H. Zhang, *Chem. Soc. Rev.*, 2012, **41**, 666-686.

22. A. Gutes, C. Carraro and R. Maboudian, *Biosens. Bioelectron.*, 2012, **33**, 56-59.

23. A. Gutes, B. Hsia, A. Sussman, W. Mickelson, A. Zettl, C. Carraro and R. Maboudian, *Nanoscale*, 2012, **4**, 438-440.

24. Y. Wang, Y. Li, L. Tang, J. Lu and J. Li, *Electrochem. Commun.*, 2009, **11**, 889-892.

25. S. Alwarappan, A. Erdem, C. Liu and C.-Z. Li, *J. Phys. Chem. C*, 2009, **113**, 8853-8857.

26. L. Wu, L. Feng, J. Ren and X. Qu, *Biosens. Bioelectron.*, 2012, **34**, 57-62.

27. D. Han, T. Han, C. Shan, A. Ivaska and L. Niu, *Electroanalysis*, 2010, **22**, 2001-2008.

28. X. Wang, M. Wu, W. Tang, Y. Zhu, L. Wang, Q. Wang, P. He and Y. Fang, *J. Electroanal. Chem.*, 2013, **695**, 10-16.

29. F. Xiao, F. Zhao, D. Mei, Z. Mo and B. Zeng, *Biosens. Bioelectron.*, 2009, **24**, 3481-3486.

30. H. You, S. Yang, B. Ding and H. Yang, *Chem. Soc. Rev.*, 2013, **42**, 2880-2904.

31. D. Zhao, Z. Wang, J. Wang and C. Xu, *J. Mater. Chem. B*, 2014.

32. J.-N. Zheng, L.-L. He, C. Chen, A.-J. Wang, K.-F. Ma and J.-J. Feng, *J. Power Sources*, 2014, **268**, 744-751.

33. J. Yan, S. Liu, Z. Zhang, G. He, P. Zhou, H. Liang, L. Tian, X. Zhou and H. Jiang,

Colloids Surf., B, 2013, **111**, 392-397.

34. J. Jiang and X. Du, *Nanoscale*, 2014.

35. N. I. Kovtyukhova, P. J. Ollivier, B. R. Martin, T. E. Mallouk, S. A. Chizhik, E. V. Buzaneva and A. D. Gorchinskiy, *Chem. Mater.*, 1999, **11**, 771-778.

36. J. Chen, B. Wiley, J. McLellan, Y. Xiong, Z.-Y. Li and Y. Xia, *Nano Lett.*, 2005, **5**, 2058-2062.

37. J.-N. Zheng, S.-S. Li, X. Ma, F.-Y. Chen, A.-J. Wang, J.-R. Chen and J.-J. Feng, *J. Mater. Chem. A*, 2014, **2**, 8386-8395.

38. Y. Li, W. Gao, L. Ci, C. Wang and P. M. Ajayan, *Carbon*, 2010, **48**, 1124-1130.

39. S.-S. Li, J.-N. Zheng, X. Ma, Y.-Y. Hu, A.-J. Wang, J.-R. Chen and J.-J. Feng, *Nanoscale*, 2014, **6**, 5708-5713.

40. F. Li, Y. Guo, R. Li, F. Wu, Y. Liu, X. Sun, C. Li, W. Wang and J. Gao, *J. Mater. Chem. A*, 2013, **1**, 6579-6587.

41. Y. Kim, Y. Noh, E. J. Lim, S. Lee, S. M. Choi and W. B. Kim, *J. Mater. Chem. A*, 2014, **2**, 6976-6986.

42. M. Liu, Y. Lu and W. Chen, *Adv. Funct. Mater.*, 2013, **23**, 1289-1296.

43. C. Xu, X. Wang and J. Zhu, *J. Phys. Chem. C*, 2008, **112**, 19841-19845.

44. J.-J. Lv, S.-S. Li, J.-N. Zheng, A.-J. Wang, J.-R. Chen and J.-J. Feng, *Int. J. Hydrogen Energy*, 2014, **39**, 3211-3218.

45. B. Viswanath, P. Kundu, A. Halder and N. Ravishankar, *J. Phys. Chem. C*, 2009, **113**, 16866-16883.

46. T.-H. Tsai, S. Thiagarajan, S.-M. Chen and C.-Y. Cheng, *Thin Solid Films*, 2012,

520, 3054-3059.

47. C. Zhou, S. Li, W. Zhu, H. Pang and H. Ma, *Electrochim. Acta*, 2013, **113**, 454-463.
48. X. Zhang, Y. Cao, S. Yu, F. Yang and P. Xi, *Biosens. Bioelectron.*, 2013, **44**, 183-190.
49. Z. Liu, X. Wang, L. Sun and Z. Yu, *Anal. Methods*, 2014, **6**, 9059-9065.
50. Y. Zheng, Z. Huang, C. Zhao, S. Weng, W. Zheng and X. Lin, *Microchim. Acta*, 2013, **180**, 537-544.

Captions

Fig. 1 (A) Low-, (B) middle-, and (C-E) high-resolution TEM images of PdAg NFs/rGO. Insets display the corresponding size distribution in image (A) and SAED pattern in image (B). The wrinkles of rGO are denoted with the purple arrows.

Fig. 2 (A) HAADF-STEM-EDS mapping images of a single PdAg nanoflower. (B) Cross-sectional compositional line profiles of two neighboring PdAg NFs. Inset shows the associated HAADF-STEM image.

Fig. 3 XRD patterns of PdAg NFs/rGO (curve a), GO (curve b), bulk Pd and Ag standard patterns.

Fig. 4 Survey (A), and high-resolution (B) Pd 3d, (C) Ag 3d, and (D) C 1s XPS spectra of PdAg NFs/rGO.

Fig. 5 Nitrogen adsorption-desorption isotherm of PdAg NFs/rGO.

Fig. 6 CV curves obtained at PdAg NFs/rGO/GCE (curve a), PdAg/GCE (curve b), rGO/GCE (curve c), Pd/C/GCE (curve d), and bare GCE (inset) in the presence of (A) 4.0 mM AA, (B) 0.2 mM DA, and (C) 1.0 mM UA with a scan rate of 50 mV s^{-1} in 0.1 M phosphate solution (pH 6.0). (D) DPV curves of PdAg NFs/rGO/GCE (curve a),

PdAg/GCE (curve b), rGO/GCE (curve c), Pd/C/GCE (curve d), and bare GCE (inset) in 0.1 M phosphate solution (pH 6.0) containing 1.1 mM AA, 22.0 μM DA, and 185.0 μM UA. DPV conditions: step potential, 4 mV; pulse amplitude, 50 mV; pulse width, 0.2 s; sample width, 0.0167 s, and pulse period, 0.5 s.

Fig. 7 DPV curves of (A) 4.0 μM DA and 40.0 μM UA, and AA of different concentrations from 1.0 μM to 2.1 mM, (B) 0.8 mM AA and 75.0 μM UA, and DA of different concentrations from 0.4 to 96.0 μM, and (C) 0.4 mM AA and 2.0 μM DA, and UA of different concentrations from 1.0 to 150.0 μM at PdAg NFs/rGO/GCE in 0.1 M phosphate solution (pH 6.0). Inset shows the corresponding linear relationship between the oxidation peak current and concentration of AA, DA, and UA, respectively. DPV conditions: step potential, 4 mV; pulse amplitude, 50 mV; pulse width, 0.2 s; sample width, 0.0167 s, and pulse period, 0.5 s.

Fig. 8 (A) DPV curves recorded for simultaneous determination of AA, DA, and UA at PdAg NFs/rGO/GCE in 0.1 M phosphate solution (pH 6.0) with AA concentrations from 1.0 μM to 4.1 mM, DA concentrations from 0.05 to 112.0 μM, and UA concentrations from 3.0 to 186.0 μM. (B-D) The linear relationship between the oxidation peak current and the corresponding concentration of AA, DA, and UA, respectively.

Fig. 9 Amperometric responses of PdAg NFs/rGO/GCE upon successive addition of

(A) 50 μM AA, (B) 10 μM DA, (C) 20 μM UA, and other chemicals to 0.1 M phosphate solution (pH 6.0). The applied potentials for AA, DA, and UA are –0.05, 0.24, and 0.37 V, respectively.

Figures

Fig. 1

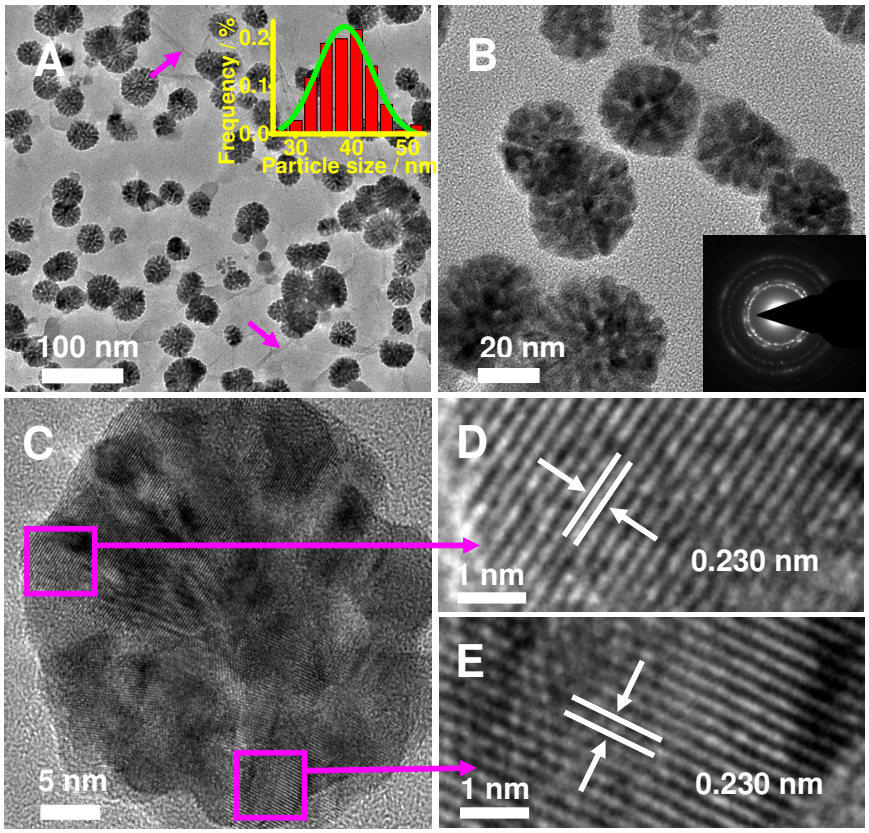

Fig. 2

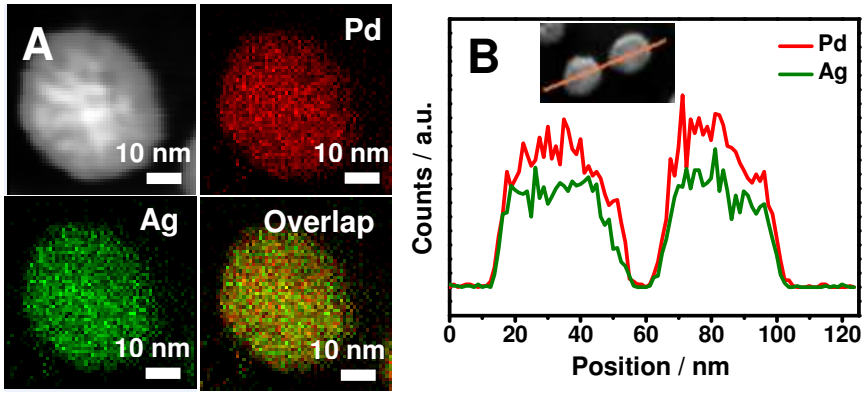

Fig. 3

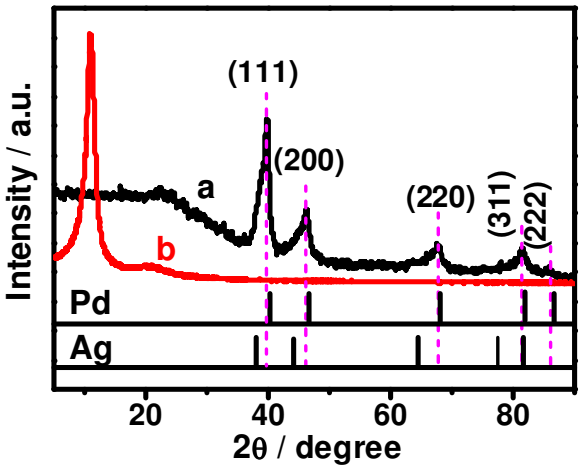

Fig. 4

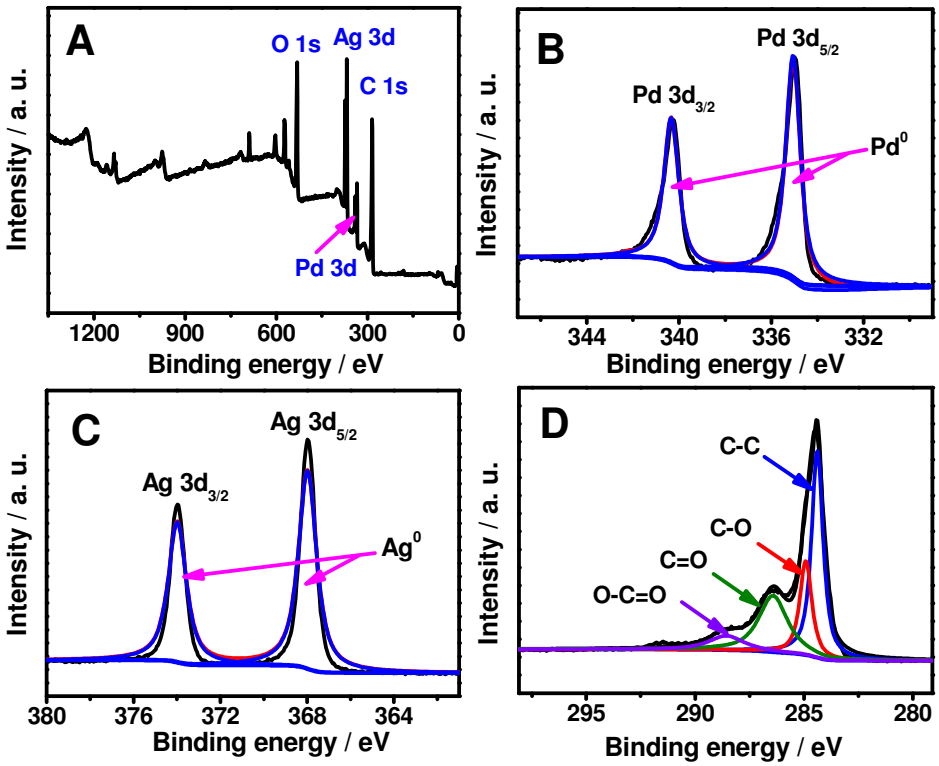

Fig. 5

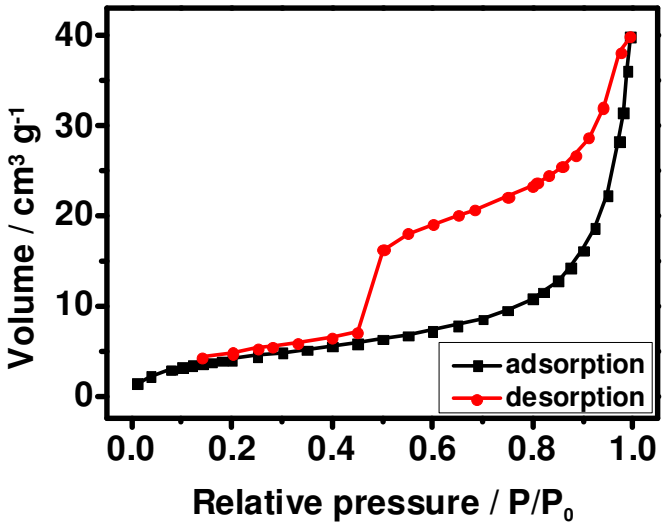

Fig. 6

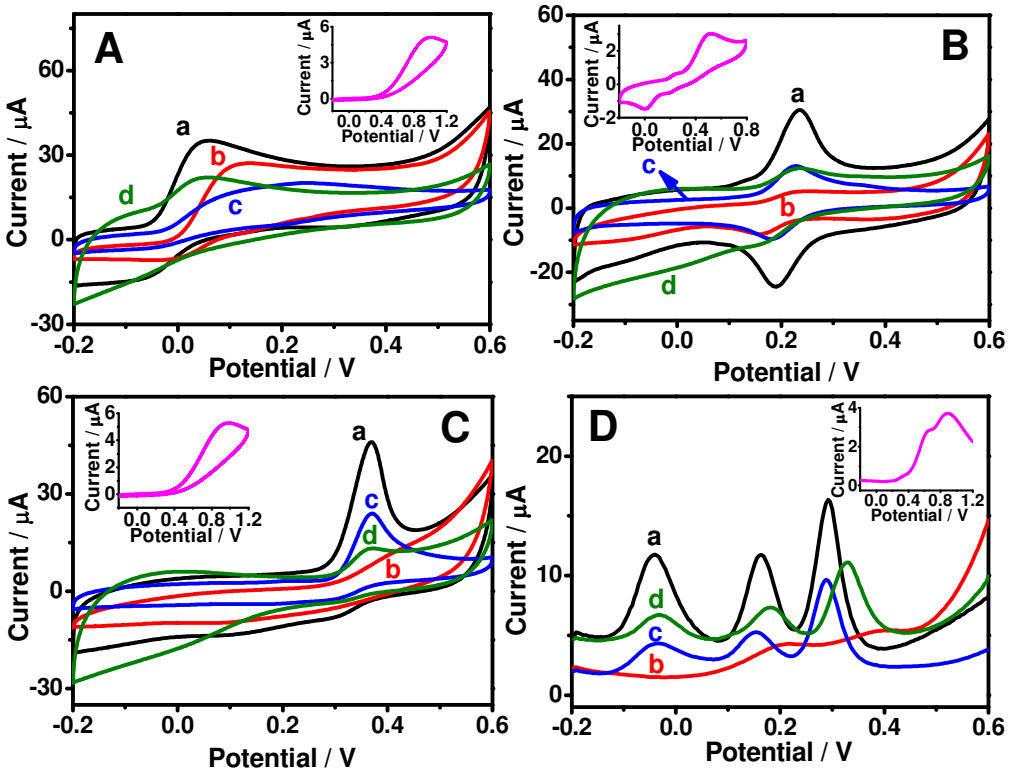

Fig. 7

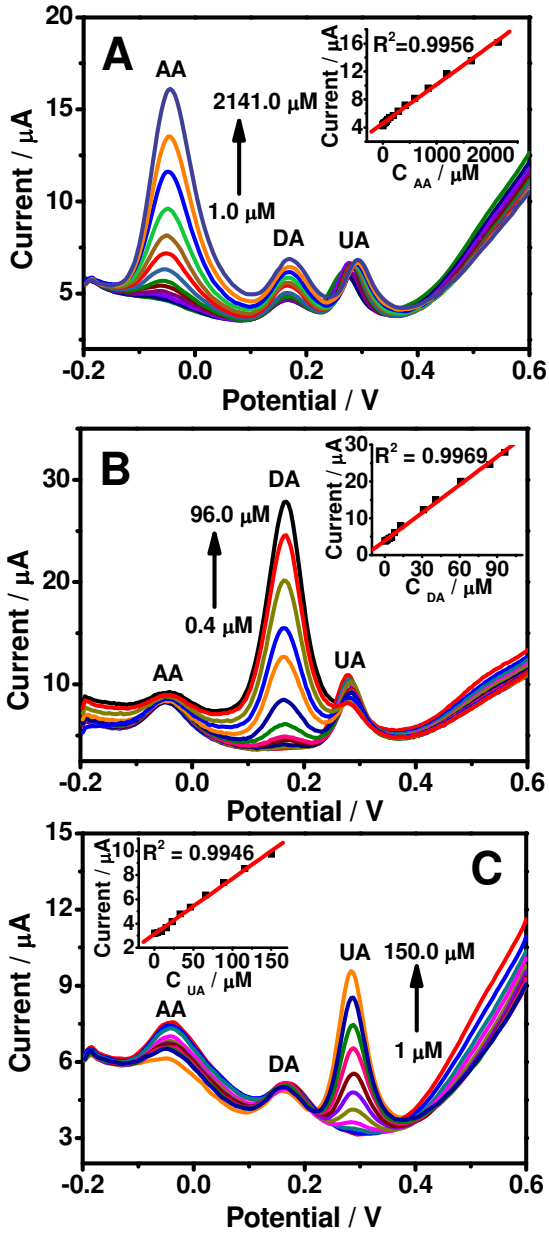

Fig. 8

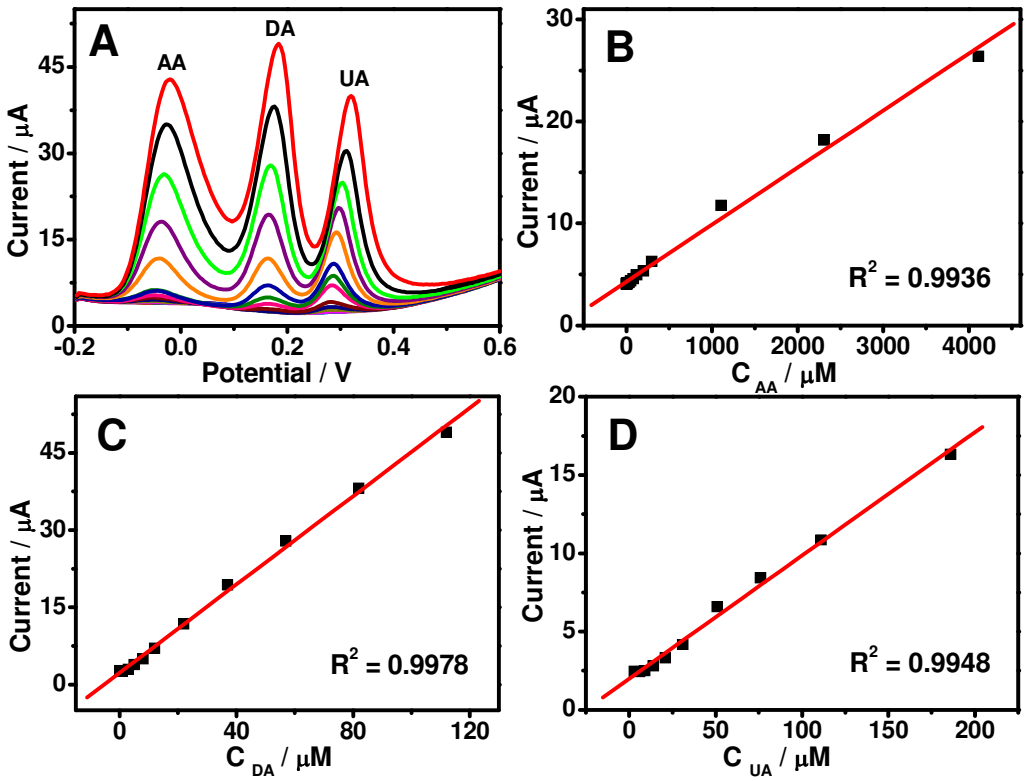

Fig. 9